Available online at www.sciencedirect.com
ScienceDirect
Journal of Solid State Chemistry 181 (2008) 1141–1148
JOURNAL OF SOLID STATE CHEMISTRY
www.elsevier.com/locate/jssc

In situ neutron diffraction study on Pd-doped $Mg_{0.65}Sc_{0.35}$ electrode material

W.P. Kalisvaart[a], M. Latroche[b,*], F. Cuevas[b], P.H.L. Notten[a,c]

[a]*Eindhoven University of Technology, 5600 MB Eindhoven, The Netherlands*
[b]*Chimie Métallurgique des Terres Rares—ICMPE—UMR7182—CNRS, 2–8 rue Henri Dunant, 94320 Thiais Cedex, France*
[c]*Philips Research Laboratories, 5656 AE Eindhoven, The Netherlands*

Received 27 November 2007; received in revised form 15 February 2008; accepted 16 February 2008
Available online 4 March 2008

Abstract

The behavior of a negative composite electrode made of Pd-doped $Mg_{0.65}Sc_{0.35}$ active material has been studied dynamically by *in situ* neutron diffraction during a complete charge–discharge electrochemical cycle starting from a virgin alloy. From the analysis of the collected diffraction patterns, phase identification, phase amounts, structural changes and cell volume evolutions have been determined as a function of the electrochemical state of (dis)charge. For the first charge, the active material shows a structural transformation from body-centered cubic (bcc) to face-centered cubic (fcc). During the following discharge, a two-phase behavior with equilibrium between a hydrogen-poor fcc phase and a hydrogen-rich one is observed. Complete discharge beyond the hydrogen-poor phase was not reached and a good electrochemical reversibility is expected between the hydrogen-poor and the hydrogen-rich fcc phases for this electrode material.

Keywords: Hydrogen storage materials; NiMH batteries; Neutron diffraction; Hydride-forming compounds; Mg–Sc system

1. Introduction

$LaNi_5$-type hydrogen storage materials have been widely used in the last decades to develop rechargeable nickel metal-hydride batteries (NiMH) [1,2]. Almost half of the small rechargeable battery market is currently devoted to this battery system and they are also currently used to power hybrid electrical vehicles (HEV). More efficient materials are needed for hydrogen storage applications in order to feed fuel cells and other promising classes of alloys are now considered. For example, beside the classical AB_5-type compounds, other phases exist in the La–Ni phase diagram [3] between 75 and 80 at% Ni such as $LaNi_3$, La_2Ni_7 and La_5Ni_{19}. Though the electrochemical properties of the binary compounds are poor, increasing interest has recently arisen for these systems due to their ability to form ternary compounds in the R–Mg–Ni system (R: rare earths) [4–9]. These phases are usually obtained by reaction of a mixture of $MgNi_2$ and RNi_5 intermetallic compounds or by direct reaction of the pure elements. Both Mg and R elements are good hydride forming compounds and this type of ternary alloy absorbs and desorbs readily hydrogen at room temperature. The possibility to prepare Mg-containing ternary intermetallic compounds allows to decrease the molar mass and therefore to increase significantly the electrochemical capacities of such electrode forming materials.

Recently, a new class of materials composed of much lighter constituents and thus revealing a much higher hydrogen storage capacity per weight than the conventional rare earth-nickel materials has been discovered and investigated at Philips Research Laboratories [10]. It was found that a specific fluorite-type (face-centered cubic (*fcc*) structure) of Mg-based compounds can store up to 4 times (close to 6 wt%) the amount of hydrogen compared to that of the conventional $LaNi_5$, making these new materials very attractive for very high capacity energy storage devices. MgH_2 has a rutile structure [11] and has been shown by Vigeholm et al. [12] to be self-limiting upon

*Corresponding author. Fax: +33 1 49 78 12 03.
E-mail address: michel.latroche@glvt-cnrs.fr (M. Latroche).

0022-4596/$ - see front matter © 2008 Elsevier Inc. All rights reserved.
doi:10.1016/j.jssc.2008.02.013

hydrogenation. However, as was proved by *ex situ* X-ray diffraction (XRD) [13], alloying Mg with Sc enables retention of the fluorite structure of ScH_2 up to 75 at% Mg leading to favorable discharge kinetics. Thin film studies on other, cheaper Mg-transition metals (TM) combinations, where the TM also forms a fluorite-type dihydride, have shown reversible capacities and charge/discharge kinetics similar to Mg–Sc. Both $Mg_{0.80}Ti_{0.20}$ and $Mg_{0.80}V_{0.20}$ showed a reversible capacity comparable to $Mg_{0.72}Sc_{0.28}$ around 6.5 wt% This confirmed the crucial role of the crystal structure in obtaining favorable transportation properties, where H-hopping is assumed to take place mainly via the largely empty octahedral interstitials in the fluorite lattice.

Previously, we reported on X-ray and neutron diffraction (ND) results on gas-phase loaded and partially unloaded Pd-doped (2.4 at%) $Mg_{0.65}Sc_{0.35}$ alloy [14]. In its as-cast form, the alloy was shown to have a partially ordered body-centered cubic (*bcc*) structure, while in the hydrided form, the Mg–Sc sublattice adopts a *fcc* structure as ScH_2. In the fully hydrided state, the D/M ratio was found to be close to 2.25. The tetrahedral sites are fully occupied (2 D/M) whereas 0.25 D/M are found to lie within the octahedral interstices. During desorption, the *fcc* structure was shown to be retained upon crossing a two-phase region by XRD. Because hydrogen atoms cannot be detected by X-rays, ND was also used to investigate the two-phase region. It was found that two *fcc* phases are in equilibrium with T-site occupancies of 1.55 and 0.85 D/M for the deuterium-rich and deuterium-poor phase, respectively.

The above-mentioned study focused mainly on the first unloading cycle, starting from a fully deuterated material and subsequently desorbing the deuterium stepwise at 300 °C. Because batteries are usually operated at RT, it is valuable to perform measurements using an electrochemical approach close to real conditions. Here, we report on the *in situ* ND analysis performed on the material $Mg_{0.65}Sc_{0.35}D_x$ during the first electrochemical charging step and subsequent discharge at room temperature in a specially designed electrochemical cell. These experiments have allowed identifying the different phases involved in the cycling behavior of this electrode material.

2. Experimental

2.1. Alloy preparation

Appropriate amounts of Mg and Sc metal pieces were hermetically sealed into a Molybdenum crucible, heated up to 100 °C above the liquidus temperature of the Mg–Sc system, ~1150 °C for this composition, and annealed for 4 days at 450 °C to give an alloy with a nominal composition of $Mg_{0.65}Sc_{0.35}$. The ingot was hammered down to pieces smaller than 5 mm and subsequently milled in a Spex 8000 ball-mill for 2 h, together with 5 at% of Pd powder (Pd is added as a catalyst). Ball-to-powder ratio was 10:1 and 2 wt% of stearic acid was added as a dispersive milling agent. The fraction with a macroscopic particle size of less than 60 μm was separated with a sieve and subsequently used to prepare the working electrodes.

2.2. Electrode assembly and electrochemical measurements

The electrode was made from about 3 g of intermetallic powder mixed with carbon black and PTFE in the weight ratio 90:5:5 as already described in [15]. This mixture was spread out in sheets of 1.5 mm thick and pressed up to 12 tons onto a $(5 \times 3.14)\,cm^2$ nickel grid, which play the role of current collector. This electrode plate was then rolled on itself to form a cylinder of about 50 mm height and 10 mm diameter. The working electrode was sandwiched between inner (∅ 8 mm) and outer (∅ 12 mm) counter-electrode cylinders made of nickel grids, with silica sheaths as separators. The working electrode was introduced in a specially designed silica cell [16] filled with electrolyte NaOD 5.5 N and pumped under primary vacuum in order to fully impregnate the working electrode with the liquid and to remove any gaseous species trapped in the material. Starting from the virgin alloy, the electrode was galvanostatically charged at $150\,mA\,g^{-1}$ (0.1 C) for 9.5 h using a HP 6177C current source. The system was then allowed to relax for 1 h in open circuit voltage (OCV) before starting the discharge at $75\,mA\,g^{-1}$ (C/20).

Standard *ex situ* electrochemical measurements were performed in a three-electrode setup. A pressed powder pellet (diameter 8 mm) consisting of the ball-milled powder and Ag powder, in a mass ratio of 1:5, was fixed onto a Ag electrode rod by means of a shrink sleeve. A Pd rod served as a counter electrode and a Hg/HgO electrode (Koslow Scientific Company) was used as the reference electrode. Charging and discharging currents were set to 100 and $50\,mA\,g^{-1}$, respectively.

2.3. Structural characterizations

XRD analysis was performed on the raw material with a Philips powder diffractometer using Cu $K\alpha$ radiation. ND data have been recorded at room temperature and ambient pressure with the position-sensitive detector (PSD) of the D1B instrument at the Institut Laue Langevin in Grenoble. The wavelength was set to 1.287 Å and the patterns were recorded every 10 min in the range 18–98° by the 400 cells of the PSD (step = 0.2° in 2θ). The diffraction patterns were sequentially refined using the program FULLPROF [17].

3. Results

Fig. 1 shows the XRD pattern of the raw material used for making the electrode. Pattern (a) represents the $Mg_{0.65}Sc_{0.35}$ alloy before ball milling. A (100) peak at 24.7° is clearly visible and such a line is not compatible with the body-centered cubic (*bcc*) cell of the structure.

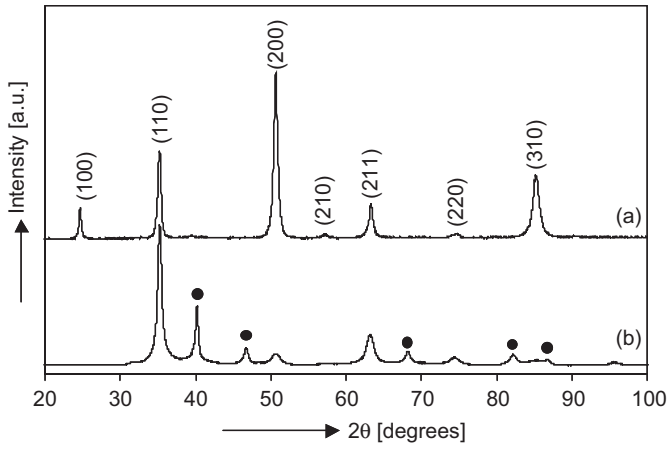

Fig. 1. XRD pattern of (a) as-cast $Mg_{0.65}Sc_{0.35}$ metal ingot, the lines are indexed in *Pm*–3*m* space group; (b) after ball milling with 5 at% Pd for 2 h. The symbols ● indicate the positions of the palladium lines.

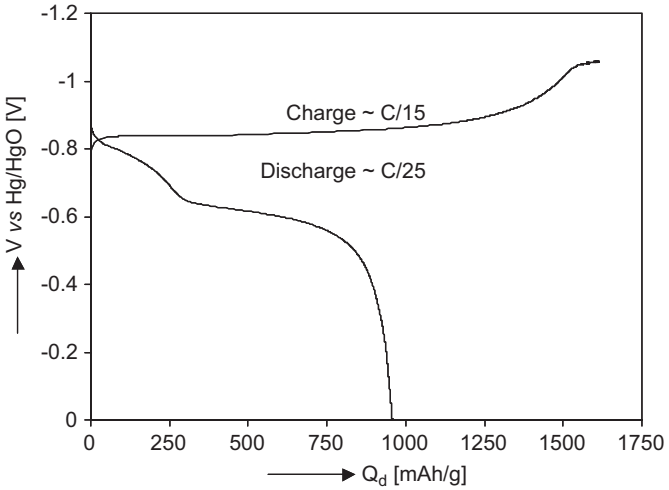

Fig. 2. Electrochemical properties of $Mg_{0.65}Sc_{0.35}$ active material in standard three-electrode electrochemical setup.

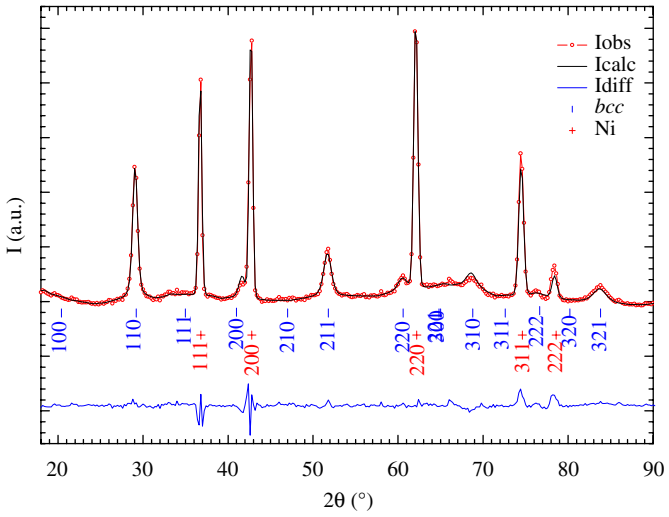

Fig. 3. ND pattern of the working electrode in dry step. The sharpest lines (+) belong to the Ni grid current collectors and the other ones (|) are attributed to the active material.

It is attributed to a partial ordering effect between the two metal sites available in the cubic structure that can be described as a pseudo-CsCl one in *Pm*–3*m* space group. However, it is worth to note that the present pattern was not obtained from powder but from the ingot after removal of the Mo-crucible. Therefore, the high intensity of the (100) reflection can be attributed to some preferential orientation. After the material has been ball-milled with Pd for 2 h, the reflections for which the sum of the indices is odd are no longer present indicating that the ordering effect has disappeared (Fig. 1b).

Prior to the *in situ* ND measurements, the active material was tested in a standard three-electrode setup. During electrochemical (dis)charge, one electron corresponds to one absorbed hydrogen atom according to

$$M + H_2O + e^- \rightarrow MH + OH^-. \quad (1)$$

From this equation and assuming an uptake of 2H/Mg and 3H/Sc, the expected charge acceptance for the alloy $Mg_{0.65}Sc_{0.35}$ corresponds to 1700 mAh g^{-1} including the extra weight due to the 5 at% of Pd. From Fig. 2, it can be seen that this calculated capacity is almost reached. Furthermore, the relative amount of charge that can be obtained at 50 mA g^{-1} is approximately the same as that reported earlier [13]. This shows that the electrochemical properties of the ball-milled material are essentially the same as those of the alloy prepared by the melting method.

The ND pattern of the working electrode material was first measured in the dry state (i.e. before filling the cell with the electrolyte). Results of the refinement are shown in Fig. 3. Beside the strong lines attributed to the Ni current collectors, reflections of the active material are observed. The Pd lines that were visible using XRD in Fig. 1 are no longer observed here. Indeed the contrast between Pd and (Mg,Sc) is much smaller with neutron than X-ray. Moreover, the amount (5 at%) is very small compared to the main phase and other ancillary equipments (silica cell, current collector, separator, etc.) making the Pd lines not detectable.

Analysis of the data in space group *Pm*–3*m* confirms the random distribution of the Mg and Sc atoms among the two available sites (Table 1) and the structure must be described in the higher symmetry space group *Im*–3*m*.

3.1. Charge of the electrode

At this stage, the electrochemical cell was filled with electrolyte and the charge process was started at 150 mA g^{-1}. Diffraction patterns were continuously recorded during charging and Fig. 4 shows a contour plot of the diffraction patterns collected during the complete charging and resting periods (10.5 h). The intensity of the *bcc* lines starts to decline right after the beginning of charging, as is clear from the contour of the (110) peak around 29° (2*θ*) in Fig. 4. After about 1 h, the lines of a *fcc*

phase can be detected, which subsequently increase in intensity until the *bcc*-phase has completely disappeared (after ~6 h).

From sequential refinement of the diffraction patterns, the relative amounts and lattice constants of the phases could be derived and are plotted in Fig. 5. Evolution of the phase amounts confirms the two-phase behavior of the system between $t = 1$ and 6 h with a progressive transformation from the *bcc* phase to the *fcc* one. However, despite a constant current rate (150 mA g^{-1}), the phase transformation deviates from linearity indicating some kinetic limitation after 3 h of charge.

The lattice constant of the *bcc* phase increases very slightly in the initial phase of charging, indicating a low D-solubility in the *bcc*-phase. After 1 h, the *fcc* phase could also be detected and its initial lattice constant is ~4.65 Å. In the next 2 h, the lattice constant of the *fcc* phase increases relatively quickly. After 6 h, the active material has almost completely disappeared (less than 3%) and the subsequent pattern refinements were conducted taking into account the resulting *fcc* phase only. The lattice constant of this latter phase continues to increase gradually upon further charging, reaching a maximum value of ~4.80 Å. This is approximately the same value as obtained in our solid–gas study for the fully deuterated material [14]. It is worth to note that a small decrease of the cell parameter of the *fcc* phase is observed during the OCV period beyond $t = 9.5$ h indicating some relaxation when the current was switched off.

The deuterium amount might also be refined from the analysis of the intensity lines of the *fcc* phase. It is important to note that the quality of the data is however affected by the small angular range, the very heavy

Table 1
Crystallographic data for the $Mg_{0.65}Sc_{0.35}$ active material obtained from powder neutron diffraction analysis using space group *Pm–3m* ($a = 3.6013(7)$ Å)

Atom	Wyckoff position	(*x*,*y*,*z*)	*B* (Å^2) (σ(*B*))	*N* (σ(*N*))
Mg	1*a*	(0,0,0,)	2.2(1)	0.68(2)
Sc				0.32(2)
Mg	1*b*	$(\frac{1}{2},\frac{1}{2},\frac{1}{2})$		0.62(2)
Sc				0.38(2)

Discrepancy factors are $R_p = 2.52\%$; $R_{\omega p} = 3.78\%$; $R_{Bragg} = 8.9\%$. Refinement of the occupancy factors for the sites 1*a* and 1*b* leads to random distribution of the element and the structure must be described as a *bcc* one in space group *Im–3m* (0.65Mg + 0.35Sc in site 2*a*).

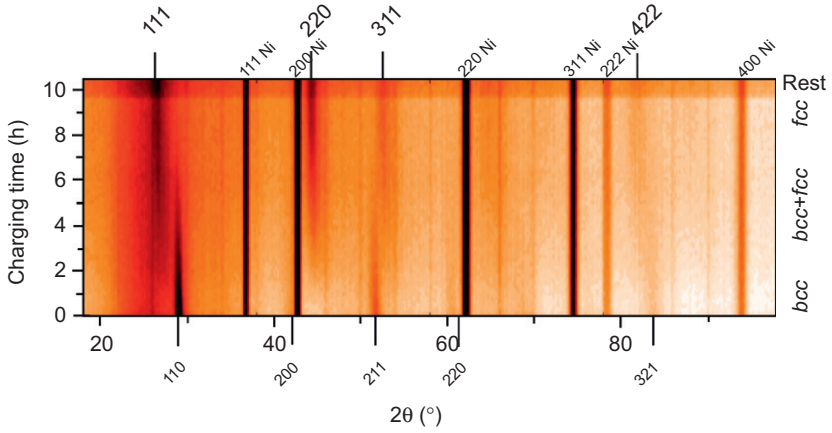

Fig. 4. 2D projection of the ND pattern intensities as function of time during charge. Increase of background contribution during the rest period (OCV) at the end of charge is clearly seen as a darker stripe.

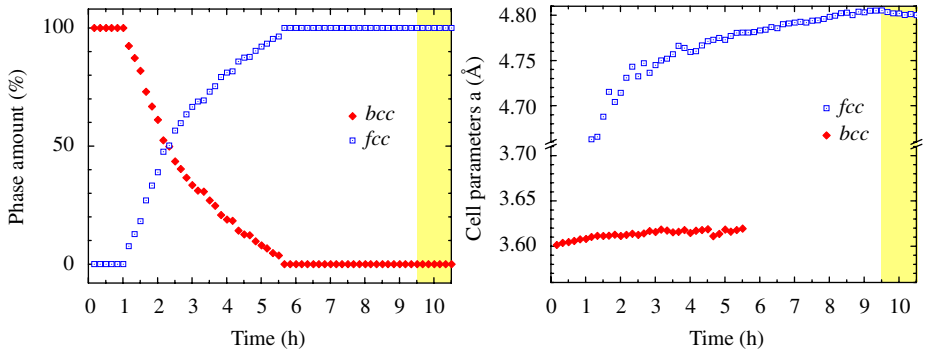

Fig. 5. Evolution of the phase amount (left) and cell parameters (right) for the *bcc* and the *fcc* phases during charge at 150 mA g^{-1} (shading areas corresponds to OCV).

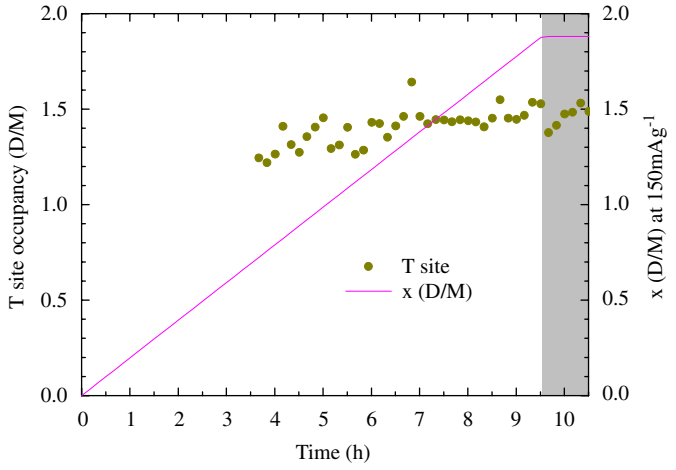

Fig. 6. Evolution of the T site occupancy for the *fcc* phase during charge at 150 mA g^{-1} (shading corresponds to OCV). For comparison, the electrochemical charge capacity ($Q = It$) converted in x (D/M) is also shown (right scale).

Table 2
Crystallographic data (*Fm*–3*m* space group, $a = 4.812$ (3) Å) of the fully charged active material $Mg_{0.65}Sc_{0.35}D_{1.50}$ obtained from refinement of neutron diffraction data during the OCV period

Atom	Wyckoff position	(x,y,z)	B (Å^2) ($\sigma(B)$)	N ($\sigma(N)$)
Mg	4*a*	(0,0,0)	0.81(3)	0.65 (fixed)
Sc				0.35 (fixed)
D(O)	4*b*	$(\frac{1}{2},\frac{1}{2},\frac{1}{2})$	–	0 (fixed)
D(T)	8*c*	$(\frac{1}{4},\frac{1}{4},\frac{1}{4})$	5.20(8)	0.75 (6)

Discrepancy factors are $R_p = 1.4\%$; $R_{\omega p} = 2.0\%$; $R_{Bragg} = 13.3\%$.

background due to silica cell, gas bubbling and heavy water, the medium resolution of the instrument and the dynamic measurement conditions. Among the two sites available in the lattice (tetrahedral T and octahedral O sites), only the T site was found to be significantly occupied (Fig. 6). The occupancy factor varies between 1.24(31) and 1.53(16) D/M (Note the large estimated standard deviation (ESD) between brackets.)

During the rest period (1 h) at the end of the charge process, diffraction patterns have been collected in a state closer to equilibrium without gas-phase evolution ($I = 0$). The diffraction pattern of the fully charged electrode has then been analyzed in order to characterize the full state of charge of the material. Metallic composition was kept fixed to the nominal value assuming random distribution of the two metals. Only the T site was found occupied with 1.50(12) D/M. The O site was not found to be significantly occupied and its occupancy factor was finally set to zero. Results of the refinement are given in Table 2 and Fig. 7. Compared to the intermetallic phase, the volume expansion upon deuteration ($\Delta V/V$) is equal to 19.3%.

The maximum value of the T-site occupation reported in Fig. 6 (1.53 D/M) is in rather good agreement with the amount of charge that has been passed through the electrode (150 mA g^{-1} during 9.5 h leads to ~1.87 D/M) if

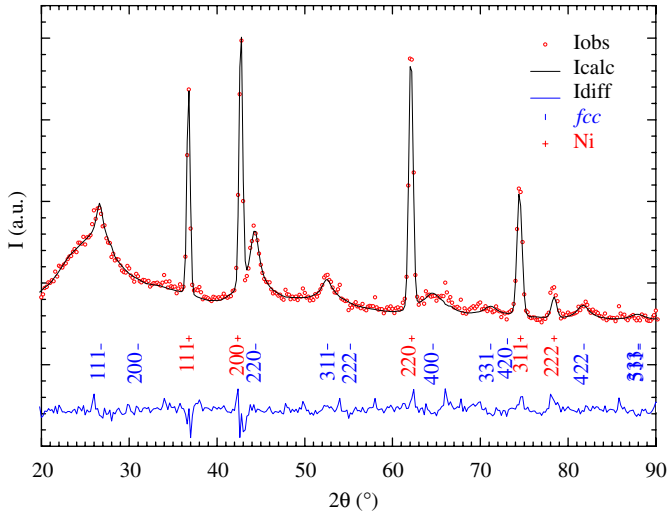

Fig. 7. -Refined neutron diffraction pattern in *Fm*–3*m* space group (measured (dots), calculated (solid line) and difference curves (below)) for the fully charged electrode collected during the OCV period. Vertical bars correspond to diffraction line positions for each phase. The pronounced hump around 25° (2θ) is due to the contribution of the electrolyte and the silica cell.

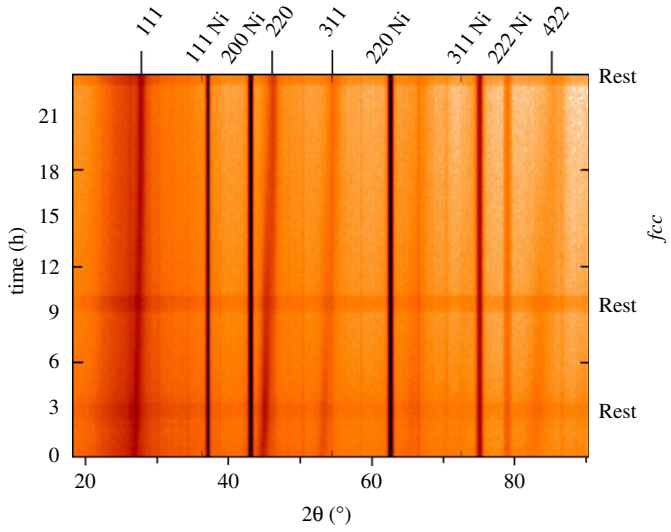

Fig. 8. 2D view of the ND pattern evolution during discharge (D/10) at 75 mA g^{-1}. Increase of background contribution during the rest periods (OCV) is clearly seen as darker stripes in the 2D map.

one assumes that gas recombination occurs at the surface of the electrode at the end of the charging process.

3.2. Discharge of the electrode

After 1 h at OCV, the electrode was subsequently discharged at 75 mA g^{-1}. At first glance, observation of the 2D view of the ND patterns (Fig. 8) does not allow to detect the presence of more than one *fcc* phase, but from solid–gas studies a two-phase equilibrium is expected. Due to the small difference in lattice parameters between those two phases (4.75 vs. 4.69 Å) and to the diffraction line width, a careful examination of the diffraction lines is

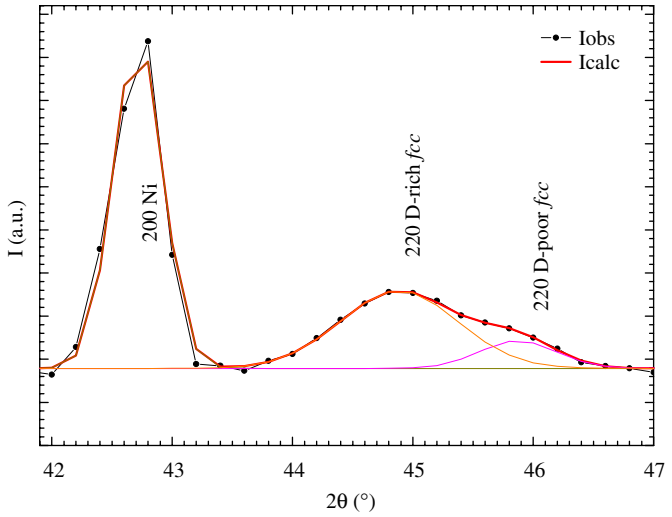

Fig. 9. Enlarged view of the 2θ region between 42° and 47° for the pattern collected during the rest period ($t = 9.16$ h). Beside the main 200 nickel line (42.8°), the strongest 220 line attributed to the D-rich *fcc* phase with 1.55 D/M is clearly seen (45°) with a shouldering attributed to the second contribution (46.06°) coming from the D-poor *fcc* phase with 0.85 D/M.

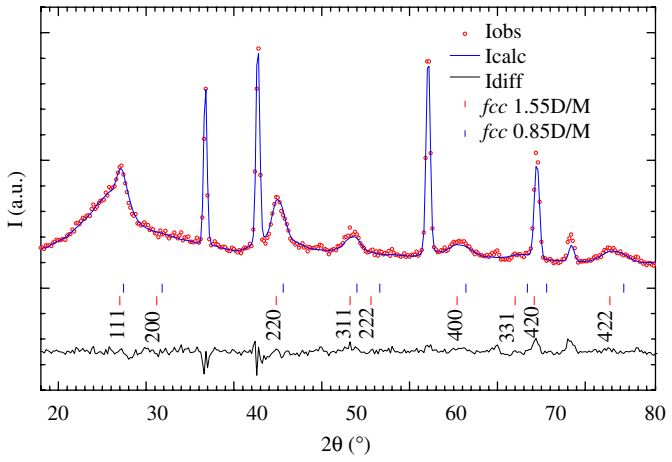

Fig. 10. Refined diffraction pattern collected during the rest period ($t = 9.16$ h) and assuming two *fcc* phases (attributed to a D-rich *fcc* phase and a D-poor *fcc* phase with 1.55 and 0.85 D/M in T sites, respectively). The pronounced hump around 25° (2θ) is due to the contribution of the electrolyte and the silica cell.

therefore necessary. A closer look at the (220) reflection revealed that it is significantly broadened in the middle of the discharging period, attesting a two-phase behavior (Fig. 9). Indeed, the ND pattern collected during a resting period, as shown in Fig. 10, after 9 h16 of discharging can be described with two *fcc* phases with lattice constants equal to 4.758 and 4.672 Å (Table 3).

Further discharge of the electrode leads to an increase in the amount of the D-poor phase. All diffraction patterns collected during the discharge were sequentially refined using 1.55 D/M in the T-site for the D-rich phase and 0.85 D/M for the D-poor phase. The variations in lattice constants and phase fractions were derived from the diffraction data and are plotted in Fig. 11.

Table 3
Crystallographic data (*Fm*–3*m* space group) from the refinement of a neutron diffraction pattern collected during a rest period (OCV) in the partially discharged state ($t = 9$ h16)

	Wyckoff position	(x,y,z)	B (Å^2) fixed	N fixed
D-rich phase $Mg_{0.65}Sc_{0.35}D_{1.55}$				
Mg	4*a*	(0,0,0)	0.25	0.65
Sc				0.35
D(T)	8*c*	$(\frac{1}{4},\frac{1}{4},\frac{1}{4})$	1.00	0.775
D-poor phase $Mg_{0.65}Sc_{0.35}D_{0.85}$				
Mg	4*a*	(0,0,0)	0.25	0.65
Sc				0.35
D(T)	8*c*	$(\frac{1}{4},\frac{1}{4},\frac{1}{4})$	1.00	0.425

The pattern was refined assuming two *fcc* phases: a D-rich (70 wt%) and a D-poor (30 wt%) one with cell parameters $a = 4.758$ (5) and 4.672 (8) Å, respectively. The fixed deuterium occupancies in T sites are equal to 1.55 and 0.85 D/M, respectively (as previously reported in 14). Discrepancy factors are $R_p = 1.44\%$; $R_{wp} = 1.94\%$; R_{Bragg} (D-rich) = 16%; R_{Bragg} (D-poor) = 16.1%.

With time, the lattice constant of the D-rich phase is found to decrease rather sharply during the first few hours of discharge, while still in a single-phase domain. It is therefore expected that the T-site occupation should decrease instead of keeping a constant value. However, the capacity extracted during the first 2 h of discharge (150 mAh g^{-1}) corresponds to ~0.18 D/M. This is more or less equal to the ESD of the T-site occupation reported in Table 2 (0.12 D/M) and does not significantly hamper the refinement. The lattice parameter of the D-rich phase varies between 4.80 and 4.73 Å, while decreasing very slightly during the transformation into the D-poor phase. The D-poor phase becomes clearly detectable after 4 h of discharge and varies in lattice parameter between 4.69 and 4.65 Å. The relative amount of the D-poor phase has increased to 90% at the end of discharge, after 22 h (24 h including 2 h of rest) and the total capacity extracted during the discharge is equal to 1650 mAh g^{-1}.

4. Discussion

The structural behavior of the $Mg_{0.65}Sc_{0.35}D_x$ electrode material has been followed in-beam during a complete electrochemical charge–discharge cycle starting from a virgin alloy. It is interesting here to compare the present work to the previous results obtained by solid–gas measurements. Firstly, it is observed that the partial ordering reported earlier was not preserved in the present material. It is indeed observed for the metal ingot just after synthesis but it disappeared after milling. Similarly, such ordering was not preserved for the deuterated phase obtained by solid–gas synthesis. That means that the stabilities of the ordered and disordered phases differ only very little and that either ball milling or hydrogenation treatment allows to stabilize the *bcc* structure (space group *Im*–3*m*).

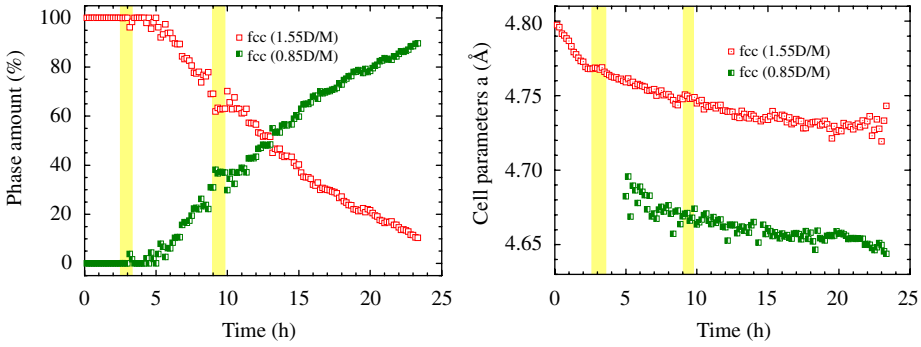

Fig. 11. Evolution of the phase amount (left) and cell parameters (right) for the two *fcc* phases during discharge at 75 mA g^{-1} (shaded areas correspond to OCV).

Starting from this equilibrated material, the first transformation from *bcc* to *fcc* was followed in-beam for the first time by ND. This phase change occurs through a two-phase domain preceded and followed by a solid solution domain characteristic for classical metallic hydride formation. The hydride formed during this first step corresponds to the D-rich phase reported in solid gas with deuterium occupying the T site (1.55 D/M). No intermediate D-poor phase was observed during loading. This is an interesting feature since solid–gas studies clearly showed a two-phase region during desorption/discharging but the present measurements seem to indicate, on charging, a different behavior during the first absorption/charging.

This picture is actually consistent with the electrochemical curve (Fig. 2), which seems to indicate a plateau-like behavior between 0 and ~700 mAh/g (~1 H/M), which would correspond to the co-existence of the *bcc* and D-rich *fcc* phase. Subsequently, the potential becomes gradually more negative, without clear indications of any other two-phase regions until the electrode is fully charged. The shape of the discharge curve is conspicuously different from the charging curve, indicating quite different behavior, as confirmed by the diffraction measurements.

Despite a long charging time in the solid solution domain of the D-rich phase, it was not possible to reach the capacity previously observed by solid gas for the fully charged hydride (2.25 D/M). Nevertheless, this Mg-based electrode exhibits good charge acceptance at the charging rate of 0.1 C. The refined deuterium amount in the D-rich phase (1.53 D/M) must be compared to the equivalent electrochemical charge (1.87 D/M). The difference can be understood if one considers that the reaction-taking place at the Ni-counter electrode is simply the oxygen-evolution reaction (OER):

$$4OH^- \leftrightarrow O_2 + 2H_2O + 4e^-. \quad (2)$$

Most of this evolved oxygen gas escapes as gas bubbles to the outside atmosphere, but part of it may react with the working electrode, where it is again reduced to OH^- ions. This reversed OER reaction consumes electrons that have to be accounted in the amount of intercalated hydrogen as derived from the charging current and time. Such reaction is indeed observed in commercial batteries at the end of charge. This oxygen recombination mechanism ensures that the partial oxygen pressure inside the NiMH battery will be kept low [2].

It is also worth to note that the lattice parameter slightly, but detectably, decreases at the end of the charge during the resting period. This effect can be related to the fact that when releasing the electrochemical potential (OCV), the equivalent overpressure is released and deuterium loss by solid gas process allowing D_2 gas evolution occurs leading to a decrease of the *D* content and thus of the cell parameter.

During discharge, the behavior of the electrochemical material is very similar to what was reported for solid gas desorption. Indeed, a two-phase equilibrium is observed between a D-rich and a D-poor *fcc* phase. Cell parameters are very comparable to those reported in [14] and remain almost constant in the two-phase domain. The diffraction patterns could be refined assuming two phases with occupancy fixed to 1.55 and 0.85 D/M in in T sites, respectively. After 22 h of discharge, the phase transformation was almost completed leading to the formation of 90% of the D-poor *fcc* phase. Full formation of this latter phase is probably the lower limit to be reached since solid gas experiments have shown that any attempt to desorb the sample beyond this H-poor phase leads to disproportionation of the hydrided phase into Mg and ScH_2.

The whole discharge capacity corresponds to 1650 mAh g^{-1}, a value significantly larger than that expected from the sole transformation from the D-rich (1.55 D/M) into the D-poor (0.85 D/M) phase (~600 mAh g^{-1}). Again part of the extracted charge is probably involved in side reactions like conversion of OH^- ions to oxygen gas following the same route than that occurring at the counter electrodes during charging. Nevertheless, from the present data, the cycling behavior of such electrode material is expected to take place reversibly between the two-reported *fcc* phase. As the discrete volume expansion between these two phases is rather small ($\Delta V/V = 5.6\%$), it is expected that few strains are generated during cycling leading to good ageing properties of the system.

5. Conclusions

The structural behavior of the Pd-doped (5 at%) $Mg_{0.65}Sc_{0.35}$ electrode material has been followed in-beam during a complete electrochemical charge–discharge cycle starting from a virgin alloy. Contrary to our previous solid–gas study, the unhydrided material exhibited a disordered *bcc* structure. During the first charge, about which no crystallographic information had been gathered yet, the active material transformed from a *bcc* to a *fcc* structure. A two-phase co-existence between the *bcc* and one *fcc* structure was found during the charge, after which the lattice constant and T-site occupation of the *fcc* phase gradually continued to increase. At the end of the charging period, the T-site occupancy was found to be 1.53 D/M whereas no O-site occupancy was found. During discharge, the coexistence between two *fcc* phases is found, in accordance with previous solid–gas experiments. In the initial stages of the discharge, the lattice parameter clearly decreased, without a statistically significant decrease in T-site occupation. Then a two-phase equilibrium takes place between a D-poor and a D-rich *fcc* phase. This differing behavior between the first charge and first discharge cycle is a remarkable finding in good agreement with the electrochemical measurements. Complete discharge beyond the D-poor phase was not possible and it is therefore assumed that reversibility occurs between the two *fcc* phases only with low cell volume variation (5.6%).

Acknowledgments

The authors wish to thank Prof. O. Isnard for its help in the neutron diffraction experiments at the Institut Laue Langevin in Grenoble. This work was financially supported by the Dutch Science Foundation (NWO) as part of the Sustainable Hydrogen program of Active Chemical Technologies for Sustainability (ACTS).

References

[1] Z.S. Wronski, Int. Mater. Rev. 46 (1) (2001) 1–49.
[2] P.H.L. Notten, in: F. Grandjean, G.J. Long, K.H.J. Buschow (Eds.), Interstitial Intermetallic AlloysKluwer, vol. 281, Academic Publishers, Dordrecht, Boston, London, 1995, pp. 150–194.
[3] D. Zhang, J. Tang, K.A. Gschneidner Jr., J. Less-Common Metals 169 (1) (1991) 45–54.
[4] K. Kadir, N. Kuriyama, T. Sakai, I. Uehara, L. Eriksson, J. Alloys Compds. 284 (1, 2) (1999) 145–154.
[5] K. Kadir, T. Sakai, I. Uehara, J. Alloys Compds. 257 (1997) 115–121.
[6] K. Kadir, T. Sakai, I. Uehara, J. Alloys Compds. 287 (1, 2) (1999) 264–270.
[7] K. Kadir, T. Sakai, I. Uehara, J. Alloys Compds. 302 (1, 2) (2000) 112–117.
[8] J. Chen, H.T. Takeshita, H. Tanaka, N. Kuriyama, T. Sakai, I. Uehara, M. Haruta, J. Alloys Compds. 302 (1, 2) (2000) 304–313.
[9] T. Kohno, H. Yoshida, F. Kawashima, T. Inaba, I. Sakai, M. Yamamoto, M. Kanda, J. Alloys Compds. 311 (2) (2000) L5–L7.
[10] P.H.L. Notten, M. Ouwerkerk, H. van Hal, D. Beelen, W. Keur, J. Zhou, H. Feil, J. Power Sources 129 (2004) 45–54.
[11] J.M. Haschke, M.R. Clark, High Temp. Sci. 7 (2) (1975) 152–158.
[12] B. Vigeholm, K. Jensen, B. Larsen, A. Schrøder-Pedersen, J. Less Common Metals 131 (1987) 133–141.
[13] W.P. Kalisvaart, R.A.H. Niessen, P.H.L. Notten, J. Alloys Compds. 417 (1, 2) (2006) 280–291.
[14] M. Latroche, W.P. Kalisvaart, P.H.L. Notten, J. Solid State Chem. 179 (2006) 3024–3032.
[15] M. Latroche, Y. Chabre, A. Percheron-Guégan, O. Isnard, B. Knosp, J. Alloys Compds. 330–332 (2002) 787–791.
[16] M. Latroche, Y. Chabre, B. Decamps, A. Percheron-Guégan, D. Noréus, J. Alloys Compds. 334 (1,2) (2002) 267–276.
[17] J. Rodríguez-Carvajal, Physica B 192 (1993) 55–69.